



OPEN Study and application on the size effect and end effect of red sandstone mechanical properties

Feng Chen^{1,2}, Jinyang Du¹, Yanhong Du¹✉, Ruxuan Li¹, Chun'an Tang³, Yishan Pan⁴ & Gen Li³

Based on the size effect, end effect, and burst tendency of rocks, this paper designs and conducts a series of uniaxial compression laboratory experiments and numerical simulation experiments to explore the influence of these factors on the mechanical properties of rocks. Dense, hard, and brittle red sandstone was used in the experiments, and specimens with different heights, cross-sectional areas, and cubic volumes were prepared. By measuring stress–strain curves, uniaxial compressive strength, and other physical and mechanical parameters, the effects of size effect on rock strength and failure modes were analyzed. Additionally, the paper discusses the influence of different-sized specimens on the rock burst tendency, introducing a parameter K to evaluate this tendency. The results indicate that the rock burst tendency of different-sized specimens remains stable around 2, with the K value of H150 specimens potentially being higher due to structural instability. Furthermore, numerical simulations using RFPA3D software were conducted to further validate the experimental results and delve into the mechanism of the end effect on the mechanical properties of rock specimens. The results indicate that the compressive strength of specimens increases with their size, and specimens of different sizes exhibit notable differences in failure modes. This paper also designs a novel "enhance strength and reduce rockburst" negative Poisson's ratio material pad based on the "cyclo-hoop effect" induced by the end effect, aiming to improve the strength of compressed components and reduce the intensity of energy release during failure. This study provides essential insights into understanding rock mechanical properties and their applications in engineering.

Keywords Size effect, End effect, Numerical simulation, Negative poisson's ratio material

Rocks are ubiquitous in underground engineering, mining, and energy development, and their mechanical properties significantly impact the stability and safety of these projects. In particular, the deformation, failure, and energy release processes of rocks under external forces are directly related to geological disasters such as rockbursts and rockbursts induced by pressure^{1–3}. Therefore, an in-depth study of rock mechanical properties, especially their burst tendency, size effect, and end effect, holds critical theoretical and engineering value for preventing and controlling geological disasters.

The heterogeneity of rocks complicates their mechanical properties, and experimental results are susceptible to various factors, including mineral composition, moisture content, temperature, and crack content. To accurately assess rock burst tendency, a comprehensive investigation of rock mechanical properties from multiple angles is essential⁴. Rock burst tendency is typically evaluated through parameters like the burst energy index, elastic energy index, and brittleness index, which provide insights into the potential for rocks to undergo catastrophic failure^{5,6}. This study focuses on rock strength and deformation properties, analyzing changes in physical and mechanical parameters like uniaxial compressive strength, elastic modulus, modulus of deformation, and failure modes through stress–strain curves. Failure modes, including tensile, shear, and mixed failures, provide critical information on the mechanisms of rock deformation and failure, which is essential for understanding and predicting rockburst events⁷.

Existing research primarily focuses on the mechanical properties of standard-sized rock specimens, with size effect studies primarily exploring the relationship between strength and size. It is generally believed that as the size increases, the uniaxial compressive strength of rocks tends to decrease^{8,9}. However, more recent

¹School of Mechanics and Engineering, Liaoning Technical University, Fuxin 123000, Liaoning, China. ²Collaborative Innovation Center of Mine Major Disaster Prevention and Environmental Restoration, Fuxin 123000, Liaoning, China. ³State Key Laboratory of Coastal and Offshore Engineering, Dalian University of Technology, Dalian 116024, China. ⁴Environmental Engineering College, Liaoning University, Shenyang 110000, China. ✉email: duyanhong1209@sina.com

studies reveal varied size effect patterns among different rocks^{10–15}, especially for brittle materials, where strength initially increases and then decreases with size^{16,17}. Current research emphasizes the significance of heterogeneity and end effect in size effect studies, as they notably impact rock strength and failure modes¹⁸. Consequently, this study designed rock specimens of varying heights, cross-sectional areas, and volumes to systematically investigate the size and end effects through uniaxial compression laboratory experiments and numerical simulations.

Furthermore, to enhance the compressive strength and shock-absorbing capacity of brittle materials like rocks, this study leverages the end effect principle to design a novel “enhance strength and reduce rockburst” negative Poisson’s ratio pad. Negative Poisson’s ratio materials have proven applications in engineering due to their superior energy absorption compared to traditional materials. For instance, the NPR (Negative Poisson’s Ratio) bolt invented by He et al. leverages the negative Poisson’s ratio characteristic of the material or structure to improve its resistance to impact, shear, and energy absorption¹⁹. Numerical simulations validate that this pad effectively enhances the compressive strength of flat specimens and absorbs energy released during failure, offering new ideas and methods to improve the stability and safety of rock engineering structures in practice. The unique deformation behavior of negative Poisson’s ratio structures, such as re-entrant, chiral, and auxetic foams, provides enhanced stiffness, strength, and energy absorption capabilities²⁰. By incorporating negative Poisson’s ratio principles into the design of rockburst prevention materials, this study aims to develop a pad that not only increases the compressive strength of rocks but also effectively absorbs and distributes the energy released during failure. Numerical simulations validate that this pad effectively enhances the compressive strength of flat specimens and absorbs energy released during failure, offering new ideas and methods to improve the stability and safety of rock engineering structures in practice.

In summary, this study aims to systematically investigate the size and end effects of rocks, revealing their influence on mechanical properties and proposing a novel negative Poisson’s ratio pad design. These findings provide theoretical support and technical reference for in-depth research on rock mechanical properties and their engineering applications.

Uniaxial compression laboratory experiments and numerical simulation experiments

Due to the heterogeneity of rocks, experimental results are susceptible to various influencing factors, such as the size, shape, mineral composition, water content, temperature, and fracture content of the rocks. However, in practical engineering, the mineral composition, water content, and ambient temperature of rocks are often constant, while the shape and size of the rocks are the main factors in assessing engineering safety and controlling engineering costs. Therefore, this paper focuses on the strength and deformation properties of rock samples in uniaxial compression experiments, combining stress–strain curves, acoustic emission, and numerical simulation to analyze the variation laws of rock’s uniaxial compressive strength, elastic modulus, secant modulus, and failure patterns with changes in rock shape and size. Consequently, dense red sandstone with relatively stable mechanical properties is selected as a reference for mechanical experiment and modeling analysis.

Laboratory experiments

This study employs high-density brittle red sandstone in conjunction with a fully automatic servo hydraulic press (as shown in Fig. 1) for a series of laboratory experiments. The red sandstone is cut into different heights, cross-sectional areas, and volumes using a cutting machine, forming three groups of rock samples, as depicted in Fig. 2. For the samples with varying heights, the cross-sectional area remains constant while the height is altered, with an increment of 25 mm. Each sample in this category measures 50 mm in both length and width, designated as H-type specimens. For the samples with varying cross-sectional areas, the height remains constant while the side length and area of the cross-section change, with an increment of 25 mm for the side length. Each of these samples has a height of 100 mm, designated as A-type specimens. For the samples with varying volumes, the

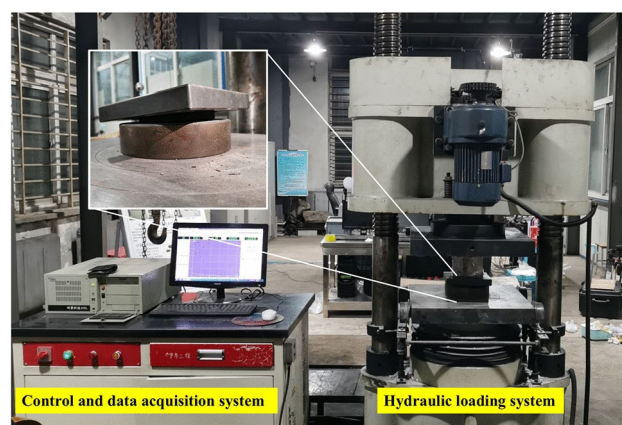


Fig. 1. Fully automatic servo press system.

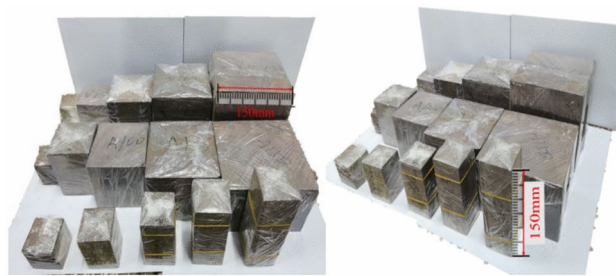


Fig. 2. Three rock samples with different types of size changes.

Sample type	Sample numbering	Sample size (mm)		
		Length	Wide	Hight
Different height	H50	50	50	50
	H75	50	50	75
	H100	50	50	100
	H125	50	50	125
	H150	50	50	150
Different cross-sectional areas	A50	50	50	100
	A75	75	75	100
	A100	100	100	100
	A125	125	125	100
	A150	150	150	100
Different volume	V50	50	50	50
	V75	75	75	75
	V100	100	100	100
	V125	125	125	125
	V150	150	150	150

Table 1. Sample type and size.

shape remains constant, with each sample being a cube, where both the edge length and volume are altered, with an increment of 25 mm for each edge length, designated as V-type specimens.

The specific dimensions and numbering of the three types of rock samples are presented in Table 1. During the rock cutting process, the cutting machine's blade is continuously cooled with water to prevent thermal damage, ensuring precise and smooth cuts. Following the cutting stage, the samples undergo meticulous grinding using a precision grinding machine equipped with fine-grained abrasives. The grinding process involves multiple passes with gradually decreasing grit sizes to achieve a highly polished surface. The duration of the grinding is carefully controlled to avoid over-grinding and to preserve the integrity of the sample's internal structure. After grinding, all samples are thoroughly cleaned to remove any residual abrasives or debris, and inspected to ensure they are free of visible fractures to the naked eye. This meticulous preparation ensures that the samples can be approximated as having the same internal structure, ready for further testing and analysis. The density of the samples is 2.425 g/cm³. All rock samples are wrapped in plastic film to prevent rock fragments from being ejected during the experiment due to sudden rupture, ensuring the integrity of the samples after failure and the safety of the experiment.

Numerical simulation experiment

To facilitate comparison with the uniaxial compression experiments of red sandstone samples of different sizes conducted in this paper, a computational model as shown in Fig. 3 was established. The dimensions of the model specimens are consistent with the actual specimen sizes. Considering the particle size of the red sandstone and computational cost, a cubic grid with a cell edge length of 1.25 mm was set, and the specimens were divided into a number of equal volume cells calculated as $(H/1.25) \times (A/1.5625)$, where H is the actual height of the corresponding specimen and A is the cross-sectional area. To ensure consistency between the simulation and the physical experiment, loading plates were set at both ends of the model, with material parameters matching those of the Laboratory experiment. The edges of the loading plates extend 10 mm beyond the edges of the specimen dimensions, with a thickness of 10 mm.

The RFPA3D program assigns values to the material strength and elastic modulus using the Weibull distribution, which approximates the variability in the strength mechanical parameters of each micro-element such as defects and grains. In this model, the mechanical parameters of the model specimens are as follows: elastic modulus $E=70,000$ MPa, Poisson's ratio $\nu=0.25$, and homogeneity degree $m=2$. To be consistent

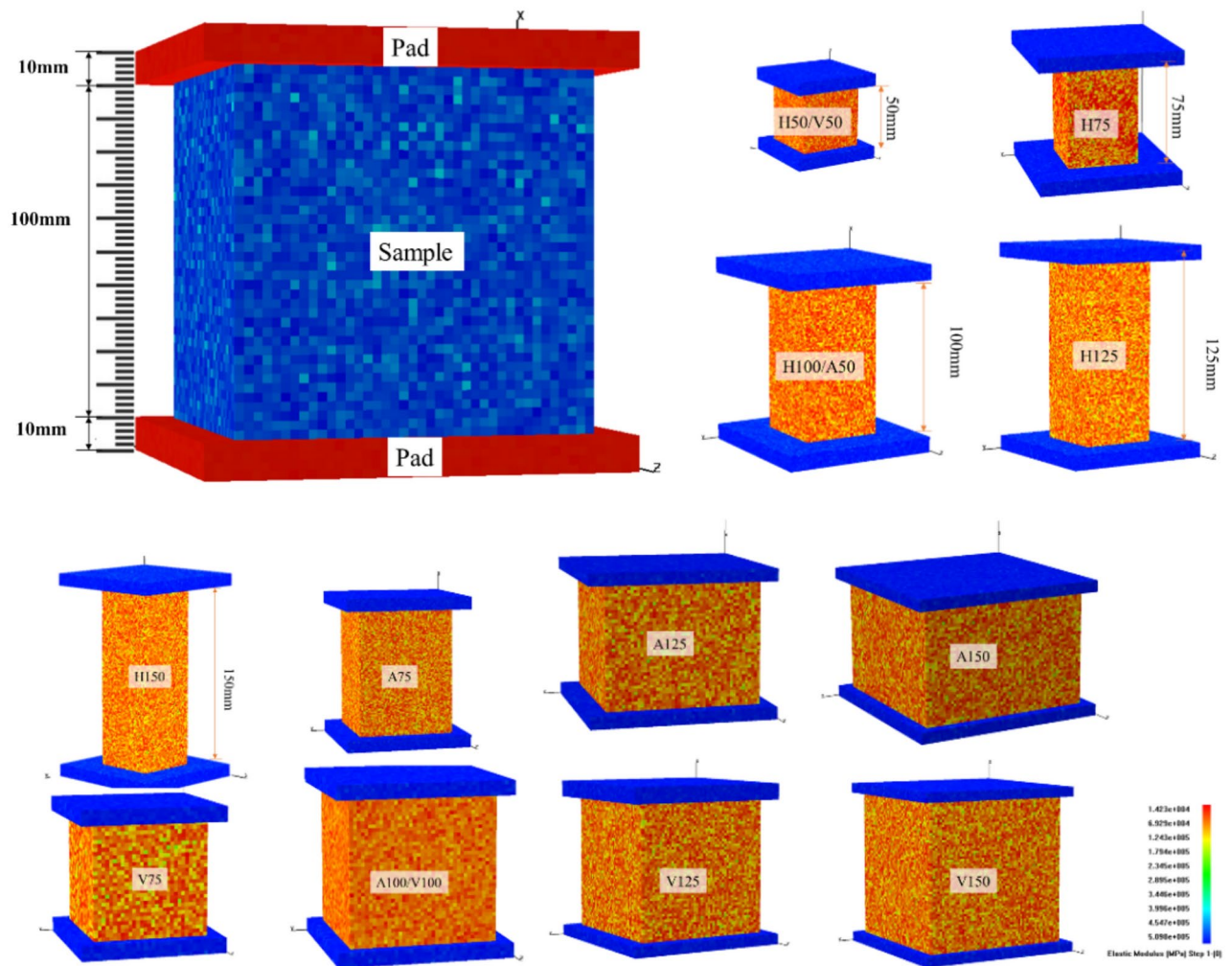


Fig. 3. Numerical simulation experiments model. 3D modeling software: RFPA^{3D}, Version number: Basic, Software link: <http://www.rfpa.cn>.

with the experimental system, loading plates are set at both ends of the specimen, with an elastic modulus E of 500,000 MPa, a strength of 4000 MPa, and a homogeneity degree m of 100. The ‘ m ’ is material structure parameter, reflecting the degree of irregularity in the distribution of defects within the material structure; the larger its value, the more uniform the material distribution. ‘ m ’ is also an average property parameter of the material.

The failure criterion for the elements is based on the Mohr–Coulomb criterion, with a friction angle of 30° and a tensile-to-compressive strength ratio C/T set to 8. The loading increment for each step is 0.002 mm, and the number of loading steps in the simulation process is set between 50 and 200, depending on the size of the model.

In the numerical model, we set key parameters such as elastic modulus, Poisson’s ratio, and homogeneity degree based on the actual physical and mechanical properties of red sandstone. These parameters were set through statistical analysis of a large amount of experimental data and literature, ensuring consistency between model parameters and actual rock properties. By adjusting the number of grids, we ensured the computational accuracy and efficiency of the model.

In the model, we set the same loading conditions as those in the laboratory experiments, including loading speed, loading method, and elastic modulus of the loading plates. These conditions were set to simulate the real experimental environment, thereby ensuring the accuracy of the model results.

After establishing the model, we conducted multiple trial calculations and continuously adjusted the model parameters and mesh division by comparing the differences between the model results and laboratory experimental results until good consistency was achieved.

To ensure the reliability of the model, we selected specimens of different sizes for numerical simulation and compared the simulation results with laboratory experimental results. The results showed that the model could accurately simulate the mechanical behavior and failure modes of specimens of different sizes, further verifying the reliability of the model.

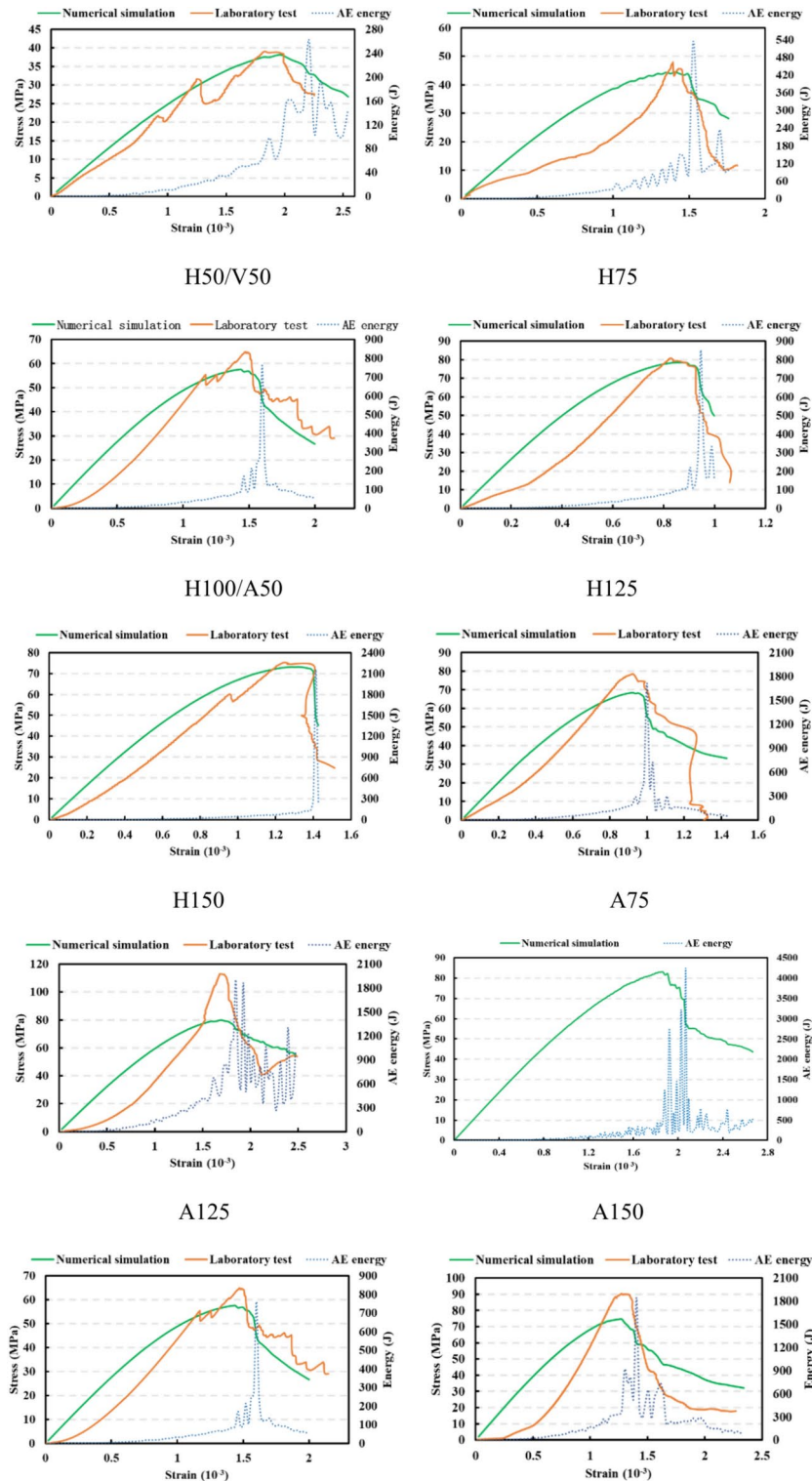


Fig. 4. Stress–strain curves and acoustic emission energy of physical experiments and numerical simulations of rock samples.

Experimental results and analysis

Experimental results

The stress–strain curves and acoustic emission energy curves of rock samples with different heights, areas, and volumes are shown in Fig. 4. Due to the A150 and V150 rock samples being able to withstand a maximum axial pressure exceeding the maximum pressure that the experimental machine can apply, their laboratory experimental stress–strain curves were not obtained. Each type of rock sample’s stress–strain curve roughly went

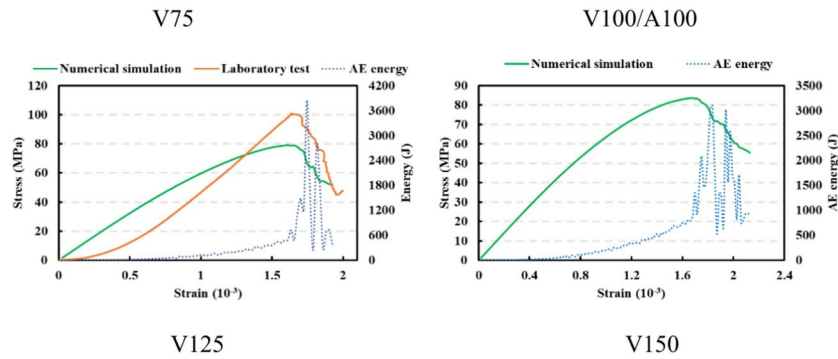


Figure 4. (continued)

through four stages: compaction, linear elasticity, plastic deformation, and failure. Compared to the laboratory experiment, the numerical simulation’s stress–strain curve did not show a significant exponential increase before the peak but exhibited a convex power growth trend, yet both showed consistent elastic modulus, peak strain, and compressive strength. Since the numerical simulation is for an ideal sample without fractures or other defects, the compaction stage is not very pronounced, making both curve growth trends reasonable.

Stress–strain curve analysis

During the uniaxial compression process of the H50/V50 sample in the laboratory experiment, the pre-peak stress–strain curve showed multi-peak fluctuations. The first peak reached 21.10 MPa and then dropped to 20.04 MPa, the second peak reached 30.97 MPa and then dropped to 25.08 MPa, and after the third peak reached 38.70 MPa, the sample structure was completely destroyed. H100/A50, H150, and V75 also showed minor fluctuations, while other samples’ stress–strain curves did not exhibit obvious multi-peak phenomena. The cause of this phenomenon may be the inevitable micro-fractures in the physical samples or the penetration of cracks causing stress redistribution within the sample.

From the numerical simulation results, the numerical simulation strength of the A125, V75, A100, and V125 specimens is slightly lower than the test strength. This is partly due to the fact that as the specimen size increases, the end frictional force increases and the end effect influence increases, causing the strength to increase. However, the end effect simulated by the numerical simulation software is caused by the depression of the spacer, ignoring the influence of end friction, resulting in a lower strength.

Relationship between strength and size

From the stress–strain curves obtained by the laboratory experiment, it can be seen that as the size increases, the compressive strength of the samples increases. As shown in Fig. 5, when the height is the controlled variable, at heights of 50 mm, 75 mm, 100 mm, 125 mm, and 150 mm, the strengths are 39.04 MPa, 47.95 MPa, 64.92 MPa, 80.78 MPa, and 75.28 MPa, respectively. The sample strength first increases and then gradually stabilizes, showing a power growth. The energy release after failure increases with the increase in sample size, and the curve gradually changes from a multi-peak to a single-peak type, indicating that the energy release becomes more sudden and intense.

When the area under compression is the controlled variable, with areas of 50×50 mm, 75×75 mm, 100×100 mm, and 125×125 mm, the strengths are 64.92 MPa, 78.61 MPa, 90.36 MPa, and 113.51 MPa,

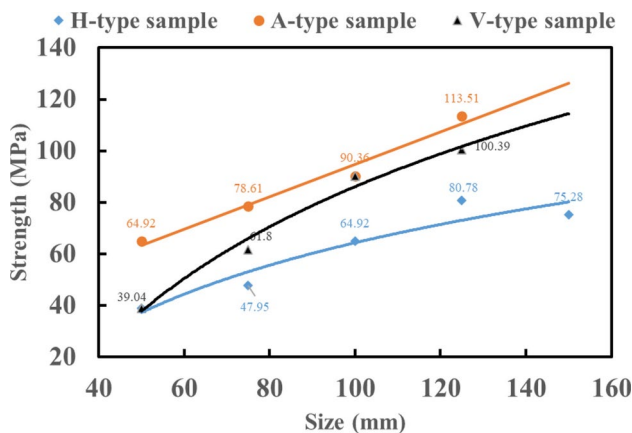


Fig. 5. Strength growth trend of samples of different sizes.

respectively, showing a linear increase. As the size increases, the energy storage capacity of the red sandstone also gradually increases, with the A150 sample's instantaneous maximum acoustic emission energy reaching up to 4240.90 J.

When the sample is a regular hexahedron and the volume is the controlled variable, with edge lengths of 50 mm, 75 mm, 100 mm, and 125 mm, the strengths are 39.04 MPa, 61.8 MPa, 90.36 MPa, and 100.39 MPa, respectively, also showing a power growth. The acoustic emission energy first increases and then decreases, and all are multi-peak curves with a main peak.

For larger-sized samples, when the height-to-width ratio is small, there is a discrepancy between the experimental and numerical simulation strength values. As can be seen from Fig. 6, the experimental strength of the V75 sample is 9.31 MPa higher than the numerical simulation, the experimental strength of the V100/A100 sample is 15.08 MPa higher than the numerical simulation, the experimental strength of the V125 sample is 22.21 MPa higher than the numerical simulation, and the A125 sample's strength is 32.11 MPa higher than the numerical simulation. One reason is the heterogeneity of the rock samples; when the sample size increases, the probability distribution of defects or fractures may be too concentrated in the critical area of failure, resulting in numerical simulation strength being lower than the physical experiments. Another reason is the influence of the end effect; as the area under compression increases, the friction force increases, and the "cyclo-hoop effect" formed at the ends of the sample increases the strength of the rock. The end effect simulated by the RFPA software is caused by the material indentation due to the mismatch of elastic modulus between the sample and the loading plate, resulting in end constraints and the end effect. The actual end effect is very complex, and factors such as the roughness of the contact surface, the area under compression, and the difference in elastic modulus between the loading plate and the sample can all affect the end effect.

The data from Fig. 6 can illustrate that when the area under compression is constant, the rougher the end, the greater the friction coefficient, and the more obvious the end constraint effect; when the end roughness is consistent, the increase in the area under compression will also enhance the effect of the end constraint, which is also the reason why the numerical simulation strength results of large-sized wide and flat samples are lower than the laboratory experiment.

Due to the large volume of the V150 and A150 samples, which exceeds the range of the testing machine, the strength values obtained by numerical simulation are 83.00 MPa and 83.70 MPa, respectively.

Combined with the linear and logarithmic function fitting analysis of the samples with area as the variable and volume as the sample, the actual strength of V150 will reach more than 110 MPa, and A150 will reach more than 120 MPa.

Theoretical foundation for the evaluation of rock burst tendency

A thorough understanding and accurate assessment of the impact tendency of rocks, especially the variation under different size conditions, is of significant importance for ensuring the safety of underground engineering (such as tunnels, mines, etc.). Through the analysis in this section, we aim to reveal the potential impact of changes in rock sample size on its tendency to burst, providing a scientific theoretical basis and safety assessment methods for practical engineering applications.

For the convenience of theoretical derivation, it is assumed that the cross-section of the tunnel is circular with an average radius of aa , as shown in Fig. 7. The distance from any point in the surrounding rock to the center O is r , and the hydrostatic pressure at infinity in the tunnel is P . Based on the axisymmetric plane strain problem, the stress, strain, and displacement of the surrounding rock are analyzed under the combined action of the original rock stress P and the support resistance P_s .

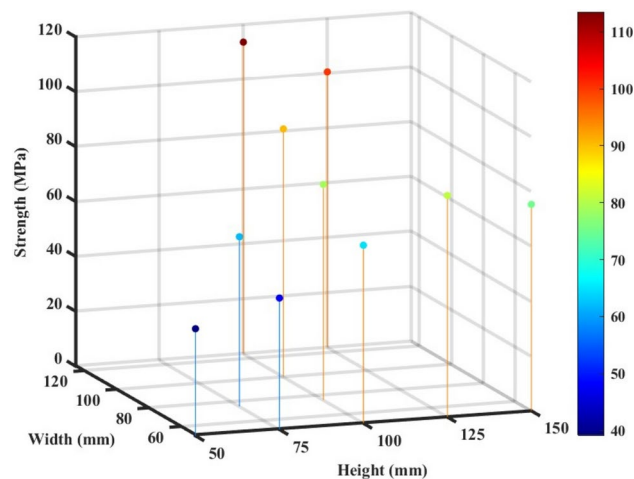


Fig. 6. Strength value of the sample in the physical experiment. The numerical simulation value is lower than that in the physical experiment. This is due to the increase of the compression area, which increases the friction force, and the enhancement of the hoop effect generated by the end effect, which increases the strength of the sample.

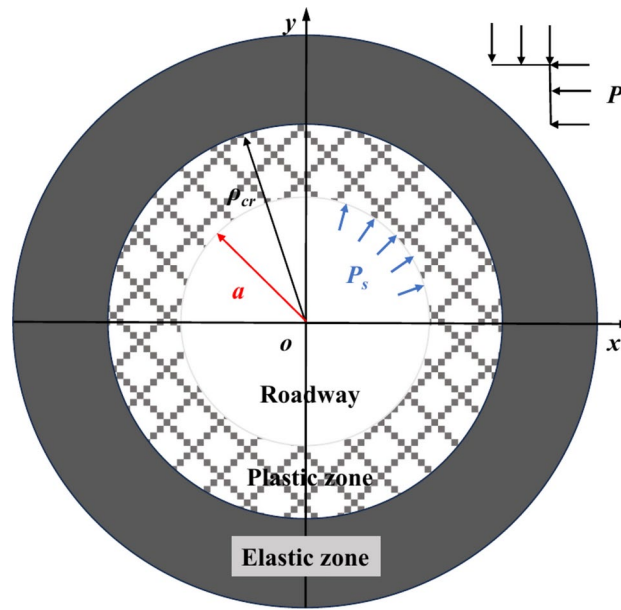


Fig. 7. Calculation model of circular section roadway.

If the far-field stress disturbance effect is considered, then the critical plastic depth and critical load can be derived from the rock burst disturbance response criterion^{21,22}.

$$\frac{\rho_{cr}}{a} = \sqrt{1 + \frac{E}{\lambda} + \frac{E}{\lambda} (m - 1) \frac{P_s}{\sigma_c}} \tag{1}$$

$$\frac{P_{cr}}{\sigma_c} = \frac{1}{m - 1} \left\{ \frac{\lambda}{E} \left[1 + \frac{E}{\lambda} + \frac{E}{\lambda} (m - 1) \frac{P_s}{\sigma_c} \right]^{\frac{m+1}{2}} - \frac{\lambda}{E} - 1 \right\} \tag{2}$$

where E is the elastic modulus; σ_c is uniaxial compressive strength; $m = \frac{1+\sin\varphi}{1-\sin\varphi}$, φ is the internal friction angle; λ is the softening modulus.

When the support resistance is not considered, Eq. (1) and Eq. (2) can be simplified as:

$$\frac{\rho_{cr}}{a} = \sqrt{1 + \frac{E}{\lambda}} \tag{3}$$

$$\frac{P_{cr}}{\sigma_c} = \frac{\frac{\lambda}{E} + 1}{m - 1} \left[\left(1 + \frac{E}{\lambda} \right)^{\frac{m-1}{2}} - 1 \right] \tag{4}$$

From Eq. (4), it can be seen that the uniaxial compressive strength, elastic modulus, and softening modulus are the key mechanical parameters affecting the critical load at which a rock burst occurs.

Assuming there is no support, according to Eq. (4), it can be inferred that the critical load for a rock burst in a tunnel is an inherent constant, depending on the properties of the rock mass itself. The lower the uniaxial compressive strength of the rock mass, the lower the critical load. Therefore, the actual load borne by the rock mass is more likely to reach the critical load, increasing the likelihood of a rock burst. Conversely, the greater the critical load of the rock mass, the more difficult it is for the actual load borne to reach the critical load, thus reducing the likelihood of a rock burst.

The strain softening characteristics of the rock mass are the fundamental internal factors affecting the occurrence of rock bursts. From Eq. (4), it can be seen that the ratio of the softening modulus to the elastic modulus is an important factor influencing the occurrence of rock bursts. Based on this, a new parameter for assessing the tendency of rock bursts is proposed. K_λ —the deformation modulus ratio.

The stress–strain curve of the rock mass can be measured through laboratory experiments, where the stress value at the peak point C is defined as the uniaxial compressive strength σ_c (see Fig. 8). The slope of the straight line during the elastic phase before the peak point C is defined as the elastic modulus E . The slope of the straight line in the softening phase after the peak point C is negative, and its absolute value is defined as the softening modulus λ . After measuring the softening modulus and the elastic modulus, the deformation modulus ratio can be expressed as:

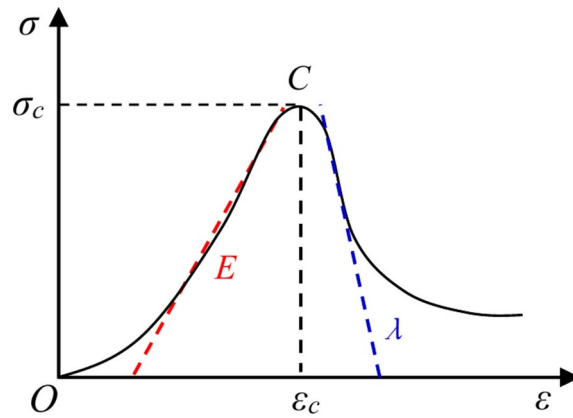


Fig. 8. Schematic diagram of stress–strain relationship of rock.

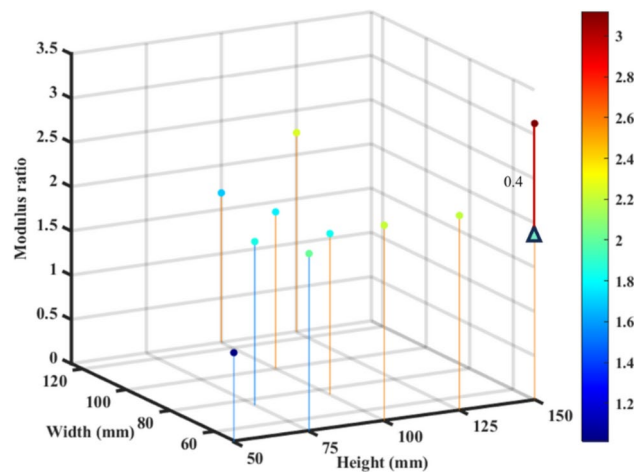


Fig. 9. Relation between the modulus ratio of the laboratory experiment and the size. When H150 reaches the peak stress, the instability failure of the pressure rod causes a sharp decline in strength and an abnormal increase in the ratio of the modulus of the laboratory experiment. The numerical simulation results show that the modulus of H150 sample is 0.4 lower than that of the laboratory experiment, and there is no sharp increase.

$$K_{\lambda} = \frac{\lambda}{E} \quad (5)$$

From the modulus ratio plot (Fig. 9), it can be observed that as the specimen size increases, the modulus ratio continuously increases. When height is the controlled variable, the modulus ratio first rises, then stabilizes, and subsequently increases again. It is noteworthy that, upon analyzing the failure mode, the H150 specimen experienced buckling failure due to column instability, which leads to a sharp decline in the post-peak phase of the stress–strain curve, thereby affecting the value of the softening modulus and resulting in a higher modulus ratio. According to numerical simulation experiments, the modulus ratio of the H150 specimen should be 2.0, indicating that the rock burst tendency of the H150 specimen does not actually undergo a significant change. Therefore, when calculating the rock burst tendency in laboratory experiments, the specimen height should be appropriately reduced to prevent eccentric compression and unstable failure, a factor that does not need to be considered in numerical simulations.

When the area under compression and volume are the controlled variables, it can be seen that there are discrepancies between some specimens' stress–strain curves and the laboratory experiments. However, upon calculation, the modulus ratios are fundamentally consistent, meaning that the modulus ratio values calculated from numerical simulations are essentially in agreement with those obtained from laboratory experiments. For instance, although the peak strength difference of the V100 specimen is 32.03 MPa, the modulus ratio difference is only 0.07.

Analysis of the mechanism of size effect

The origins of the size effect in rocks are intricately complex, involving the presence of micro-fractures and micro-pores, as well as the diversity, proportion, distribution pattern, and particle size of mineral components, which

together constitute the significant heterogeneity of rocks. In addition, technical details during the experimental process, such as the roughness matching between the specimen and the testing machine's end surface, and the difference in elastic moduli between the two, also profoundly affect the manifestation of the size effect. These causes can be broadly categorized into two main types: the inherent heterogeneity of the rock and the inevitable end effects in experimental operations.

It is worth noting that while research on the heterogeneity of rocks is fraught with uncertainty and randomness, and even specimens of the same size and composition can yield vastly different results in uniaxial compression experiments, the study of end effects is relatively controllable and quantifiable. Most critically, research indicates that when the specimen size crosses a certain critical point, the end effect becomes the primary factor influencing the size effect.

End effect

In simple terms, the end effect is the significant impact on the measured strength values during the uniaxial compression process due to the restraint of the frictional force of the testing machine's loading plates at both ends of the specimen, preventing free lateral expansion. The conditions for its occurrence are as follows: the specimen is under uniaxial compression, the stiffness of the loading plates must be higher than that of the specimen, and there must be sufficient friction between the specimen's end surface and the loading plates, leading to the restriction of the Poisson effect, the formation of a conical compression zone at both ends, and placing the rock in this area under triaxial compression. As the height of the specimen increases, the conical compression zone separates from the overlapping state, the middle part of the specimen returns to uniaxial compression, while both ends remain under triaxial compression. This change is directly related to the stress distribution pattern within the specimen^{23–25}.

To analyze the influence of end constraints on horizontal stress, a mechanical model is established as shown in Fig. 10:

$$\sigma_x = \sigma_y = E_r \left(\frac{u_{x,r} - u_{x,m}}{D} \right) \quad (6)$$

$$u_{x,r} = \varepsilon_{x,r} D, u_{x,m} = \varepsilon_{x,m} D_m \quad (7)$$

$$\varepsilon_x = -\nu \varepsilon_z = \frac{-\nu \sigma_z}{E} \quad (8)$$

The horizontal stress induced by end constraints is given by:

$$\sigma_x = -\frac{E_r \sigma_z}{D} \left(\frac{\nu_r}{E_r} - \frac{\nu_m}{E_m} \right) \quad (9)$$

In Eq. (9), σ_x , σ_y , and ε_x , ε_y are the stresses and strains in the x and y directions, respectively. ε_z represents the axial strain. ν_r and ν_m are the Poisson's ratios of the rock specimen and platen, while E_r and E_m are their respective elastic moduli. D represents the side length at the end of the rock specimen.

To effectively mitigate the end effect, various measures can be taken, such as lubricating the ends of the specimens (e.g., by placing mica sheets, applying lubricants), setting up padding blocks, or increasing the length of the specimens^{26,27}. In the sampling and processing of red sandstone, the flatness of the upper and lower end

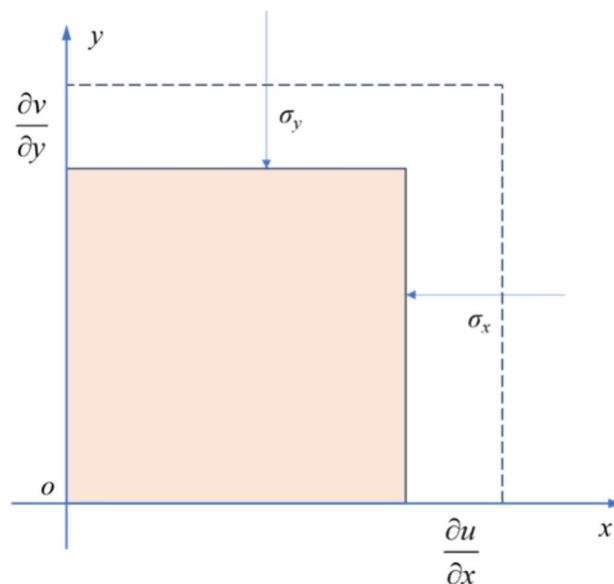


Fig. 10. The mechanical model of the end effect influenced by lateral constraints.

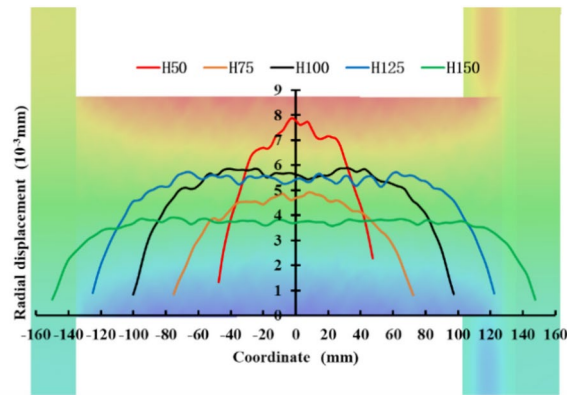


Fig. 11. Radial displacement and displacement cloud diagram at different positions of the H-type specimen's end effect.

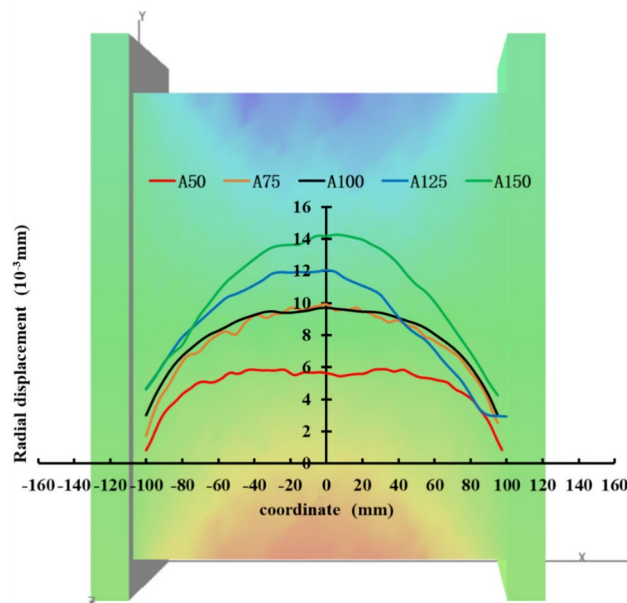



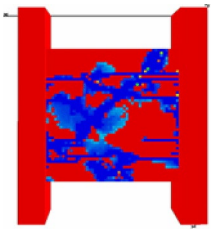

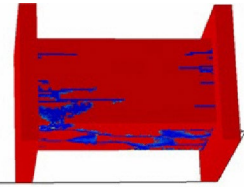

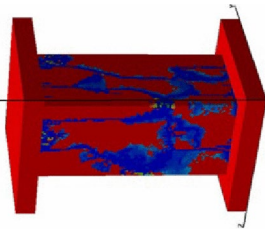

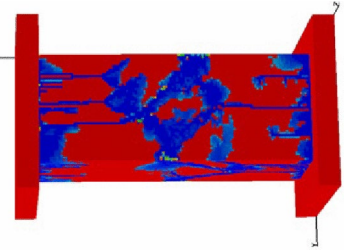
Fig. 12. Radial displacement and displacement cloud diagram at different positions of the A-type specimen's end effect.

surfaces is particularly crucial as it directly affects the effectiveness of reducing the end effect. The mechanism of the end effect involves the frictional force between the specimen and the loading plate and the indentation constraint of the loading plate on the specimen, which are determined by the friction coefficient, pressure, and the difference in elastic modulus between the specimen and the loading plate. For specimens from the same batch, if the surface treatment method is uniform, the friction coefficient will be similar. At this time, the strength of the wide and flat specimens increases with the increase in the area under compression, reflecting that the force and frictional force acting on the surface of the specimen are enhanced. Meanwhile, the indentation of the loading plate surface is intensified, further amplifying the impact of the end effect.

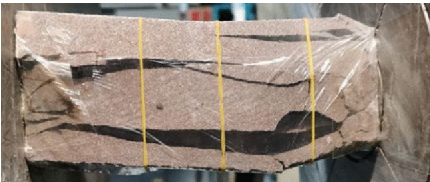
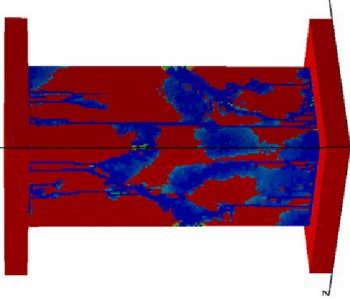

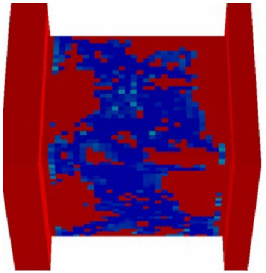

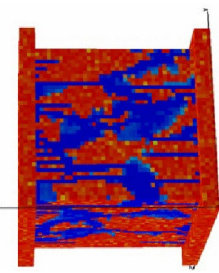
Relationship between end effect and sample size

The data from Figs. 10, 11 and 12 show that the end effect has a very significant impact on the radial deformation of rocks. The closer to the end, the greater the influence of the end effect and the greater the rate of displacement change. The end effect has the greatest impact on specimens with smaller height dimensions.

For specimens with H (height) as the variable, as the height increases, the radial displacement at the center of the specimen gradually decreases. At a height of 50 mm, the central displacement is close to 8.0×10^{-3} mm, and it rapidly decreases near both ends; while at a height of 150 mm, the radial displacement at the center is reduced to 3.8×10^{-3} mm, much lower than that of the H50 specimen, with a more gentle displacement change in the center and a smaller rate of change near both sides. It can also be seen that for H100 and H125 specimens, the

Rock sample type	Failure mode Laboratory experiments	Numerical simulation	Failure form	Failure mechanism
H50			Vertical splitting occurs concurrently with single-plane shear failure	The specimen has a small volume, and the combined effects of rock heterogeneity and end effects make the failure mechanism extremely complex
H75			Dominantly characterized by vertical splitting	As the specimen size increases, the influence of the end effect on the central part of the specimen gradually decreases, while the number and probability of internal defects in the rock increase
H100				
H125			Both ends initiate with vertical splitting, while the middle part of the specimen experiences single-plane shear failure	

Continued

Rock sample type	Failure mode Laboratory experiments	Numerical simulation	Failure form	Failure mechanism
H150			Both ends initiate with vertical splitting, the middle part of the specimen undergoes single-plane shear failure, and concurrently, the middle part experiences buckling failure akin to an Euler column instability	
A75			Vertical splitting occurs concurrently with single-plane shear failure	The wide and flat specimens are overall under the influence of the end effect, and under the influence of the cyclo-hoop effect, they are in a state of confinement. As the size increases, they exhibit plastic failure
A100				

Continued


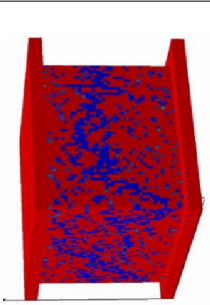

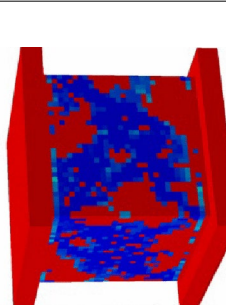

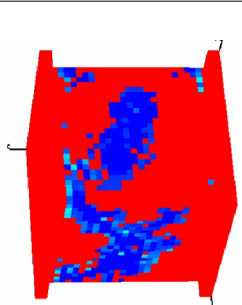
Rock sample type	Failure mode Laboratory experiments	Numerical simulation	Failure form	Failure mechanism
A125			X-shaped conjugate shear failure	
V75				
V125				

Table 2. Failure results of different types of red sandstone.

central radial displacement stabilizes at about 5.5×10^{-3} mm, indicating that the size effect is weakened when the rock specimen reaches this size category.

For specimens with A (area under compression) and V (area under compression and height) as variables, as the area increases, the radial displacement significantly increases, and the influence of the end effect covers the entire specimen. The maximum displacement of the A150 specimen is 2.3 times that of the A50 specimen. For V specimens with the same size span, V150 is only 1.78 times that of V50. For H specimens with the same size span, H50 is 2.0 times that of H150. This indicates that the increase in height weakens the impact of the end effect, while the increase in area and volume enhances the impact of the end effect.

Whether it is the height-variable size specimens or the area and volume-variable specimens, when the size reaches about 100 mm, the data change is not significant, that is, the specimen size of 100 mm shows a weaker size effect. In contrast, specimens of 150 mm and 50 mm sizes exhibit a strong size effect.

Fracture pattern analysis

Under the influence of the end effect, the failure of red sandstone is primarily a compound type of failure involving tensile and shear fractures. Figure 12 shows that the results of numerical simulation of the failure are highly consistent with those of the laboratory experiments.

During the numerical simulation process, the rock first experiences vertical splitting cracks at both ends, with numerous and fine initial cracks accompanied by low acoustic emission energy and fewer counts; as the load continues to be applied, the initial cracks at both ends extend and connect, forming through-going cracks, with shear cracks appearing in the middle of the specimen; when the ultimate strength is reached, both shear and splitting cracks have fully extended, and the number and energy of acoustic emissions reach their maximum values.

For specimens with a smaller height, shear failure is the main form of failure, affecting the entire specimen with shear cracks. As the height increases, the vertical splitting cracks become larger and more numerous, and the shear cracks gradually concentrate in the middle of the specimen. When the specimen height reaches 150 mm, Fig. 12 shows that the failure is basically vertical splitting, with bending and breaking in the middle of the specimen, similar to the buckling instability state in material mechanics.

To further illustrate the failure results of different types of red sandstone, Table 2 is provided below, summarizing the key observations:

Design of "enhance strength and reduce rockburst" novel negative poisson's ratio pad

Based on the research findings of this paper, wide and flat specimens as well as regular hexahedral specimens exhibit a size effect under uniaxial compression, where the larger the volume and the area under compression, the higher the strength, the greater the energy storage capacity, and the more intense the energy release upon failure, making them the most dangerous brittle load-bearing components. According to the study of the end effect, the reason for the increase in strength of wide and flat specimens as the size increases is the "cyclo-hoop effect" caused by the end effect. Based on this principle, a novel energy-absorbing pad with a negative Poisson's ratio, as shown in Fig. 13, can be designed. This composite structure can effectively enhance the strength of the compressed rock, and the porous negative Poisson's ratio material can effectively absorb the impact energy brought about by the rock's destruction, achieving the effect of "enhance strength and reduce rockburst". The negative Poisson's ratio pad takes an example of micro-NPR steel plates with a microscopic negative Poisson's ratio effect, which do not exhibit obvious necking during macroscopic tension²⁸, and fiber-reinforced composite materials with micro-porous structural units having concave corners can also be used to create negative Poisson's ratio pads²⁹⁻³¹. Regarding the mechanical parameters of the pad, it is known from the literature³² that NPR steel can reach a maximum strength of 1459 MPa, and the Poisson's ratio may be affected by various factors such as material preparation process, microstructure, and experiment conditions. Compared with ordinary steel (with a Poisson's ratio of about 0.25), the ratio of transverse strain to longitudinal strain of NPR steel is approximately around -0.25 when subjected to tension.

To verify the mechanical performance and actual effectiveness of the negative Poisson's ratio pad, taking the A125 specimen as an example, the specimen with the new type of pad added was modeled and analyzed using the RFPA3D software (as shown in Fig. 14), with the new negative Poisson's ratio pad having a thickness of 10 mm and a Poisson's ratio of -0.25. By comparing with the numerical simulation experiment results of the A125 specimen without the new pad, it was found that the new pad can effectively improve the load-bearing capacity of the target specimen. Figure 15 shows that the strength of the new pad reached 101.33 MPa, which is 1.3 times the compressive strength of the same type of specimen, and the maximum acoustic emission energy was reduced by 81 J compared to the specimen without a pad. The energy curve has no obvious prominent points or dominant peaks, indicating that the energy of the specimen with the new negative Poisson's ratio pad is slowly and evenly released upon failure, which can be detected in time in case of danger for early warning and avoidance.

The design of the novel negative Poisson's ratio pad, when used in the scenario of mine pillars as a support system, can significantly enhance support stability, reduce impact and vibration, extend service life, and improve safety. These practical functions are of great importance for ensuring the safe production of mines and the life safety of personnel (Fig. 16).

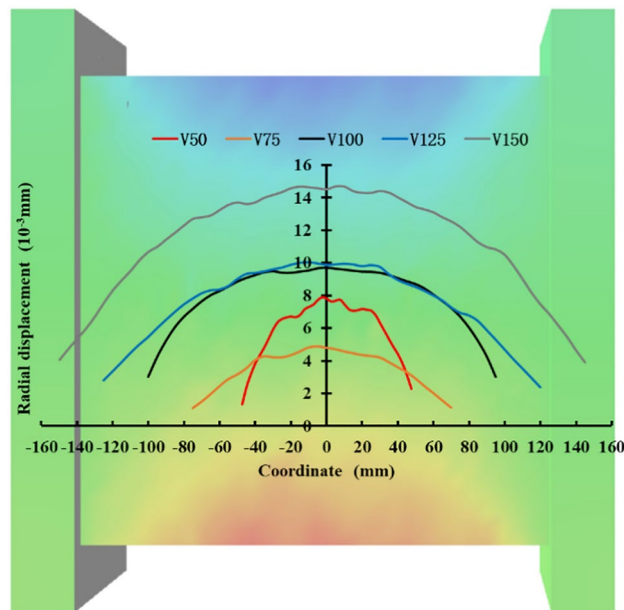


Fig. 13. Radial displacement and displacement cloud diagram at different positions of the V-type specimen's end effect.

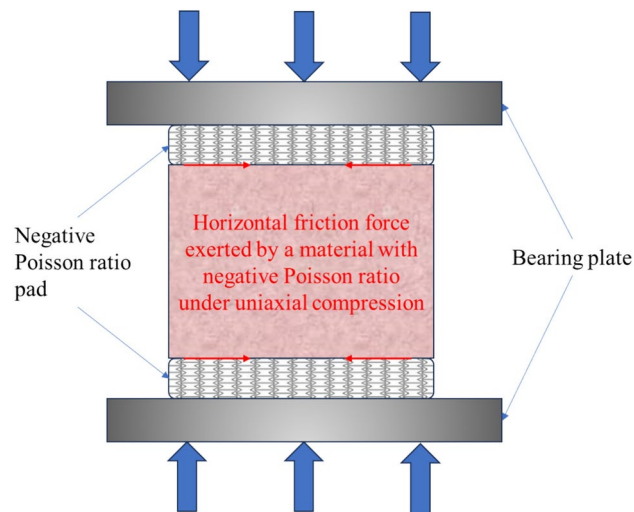


Fig. 14. Schematic diagram of the design for the novel negative Poisson's ratio pad.

Conclusions

1. The research findings indicate that as the specimen size increases, the compressive strength exhibits a trend of initially increasing and then stabilizing, rather than the traditionally perceived monotonic decrease. Specifically, when the specimen height or volume is the controlled variable, the compressive strength shows a power-law growth trend; when the area under compression is the controlled variable, the strength increases linearly. This discovery challenges existing theoretical understandings of rock size effects and reveals the complex mechanical behavior of brittle materials under size variations.
2. This study also found that specimens of different sizes exhibit significant differences in failure patterns, especially that larger-sized specimens release energy more abruptly and violently upon failure. Comparative analysis between numerical simulation and laboratory experiments revealed that the end effect significantly influences the strength of rocks, with the "cyclo-hoop effect" formed at the specimen ends enhancing the rock strength as the area under compression increases.
3. Based on the aforementioned research, this paper innovatively designed a novel "enhance strength and reduce rockburst" negative Poisson's ratio material pad. The pad leverages the "cyclo-hoop effect" caused by the end effect, aiming to increase the strength of compressed components and reduce the intensity of energy release during failure. Numerical simulation validation demonstrates that the pad can effectively enhance the

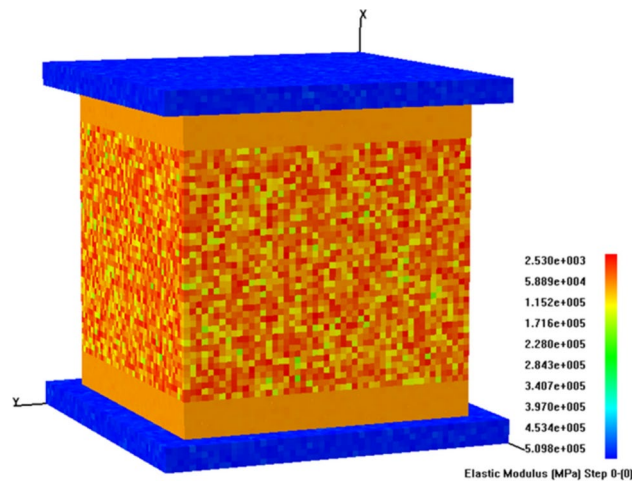


Fig. 15. Numerical simulation diagram of the new negative Poisson ratio pad. 3D modeling software: RFP3D, Version number: Basic, Software link: <http://www.rfpa.cn>.

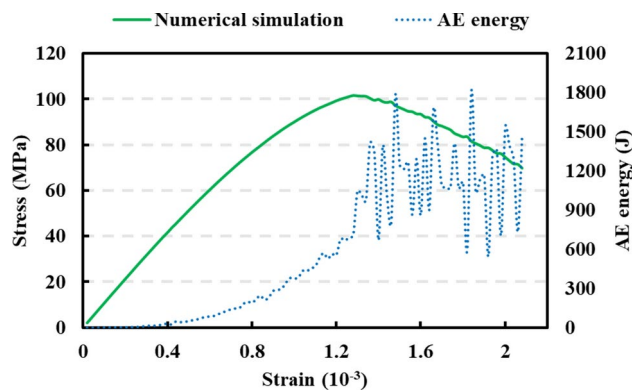


Fig. 16. Stress–strain curve and acoustic emission energy relationship of A125 after the addition of a new negative Poisson's ratio pad.

compressive strength of wide and flat specimens and effectively absorb the energy released during specimen failure, providing new ideas and methods for improving the stability and safety of rock engineering structures in practical engineering applications.

Data availability

The data used to support the findings of this study are available from the corresponding author upon request.

Received: 1 November 2024; Accepted: 28 January 2025

Published online: 08 February 2025

References

- Pan, Y. S., Li, Z. H. & Zhang, M. T. Distribution, type, mechanism and prevention of rockburst in China. *Chin. J. Mech. Eng.* **22**(11), 1844–1851 (2003).
- Chen, F. Numerical simulation study of overly strata crack evolution process influence by mining. *Chin. J. Mech. Eng.* **25**(2), 60–64 (2014).
- Mazaira, A. & Konicek, P. Intense rockburst impacts in deep underground construction and their prevention. *Can. Geotech. J.* **52**(10), 1426–1439 (2015).
- Wang, X. et al. Experimental and numerical investigations on damage mechanical behaviors of surrounding rock-backfill composite under uniaxial compression. *Constr. Build. Mater.* **417**, 135210 (2024).
- Xuefeng, S., Yong, L.,* Fengqiang, G., Jiancheng, H. & Kaifeng, H. Temperature effect of rockburst in granite caverns: insights from reduced-scale model true-triaxial test. *Geomech. Geophys. Geo-Energy Geo-Resour.*, 10: 26 (2024).
- Xuefeng, S., Zilong, Z., Xibing, L., Guansheng, Y., Yong, L., Lihai, T. & Kaifeng, H. Influences of maximum principal stress direction and cross-section shape on tunnel stability. *J. Rock Mech. Geotech. Eng.*, (2024).
- Yong, L., Jiancheng, H.,* Xuefeng, Si.,* Feng, L. & Wuxing, W. An energy-based method for uniaxially compressed rocks and its implication. *J. Rock Mech. Geotech. Eng.*, (2024).
- Pérez-Rey, I. et al. Size effects on the tensile strength and fracture toughness of granitic rock in different tests. *J. Rock Mech. Geotech. Eng.* **15**(9), 2179–2192 (2023).

9. Huang, H., Shen, J., Chen, Q. & Karakus, M. Estimation of REV for fractured rock masses based on geological strength index. *Int. J. Rock Mech. Min.* **126**, 104179 (2020).
10. Xiaoyu, L., Zheng, Y. & Huimei, Z. Energy balance size effect model of compressive strength for quasi-brittle materials. *J. Theor. Appl. Mech-pol* **54**(6), 1613–1629 (2022).
11. Chen, F., Du, J., Lv, J., Tang, C. & Pan, Y. Study on the size effect of rock burst tendency of red sandstone under uniaxial compression. *Sci. Rep.* **14**, 16402 (2024).
12. Chen, F., Du, J., Tang, C., Du, Y. & Pan, Y. Analysis of size effect and its influencing factors of brittle red sandstone with different heights. *Sci. Rep.* **14**, 15773 (2024).
13. Bahrani, N. & Kaiser, P. K. Numerical investigation of the influence of specimen size on the unconfined strength of defected rocks. *Comput. Geotech.* **77**, 56–67 (2016).
14. Zhang, Q., Zhu, H., Zhang, L. & Ding, X. Study of scale effect on intact rock strength using particle flow modeling. *Int. J. Rock Mech. Min.* **48**(8), 1320–1328 (2011).
15. González-Fernández, M. A., Estévez-Ventosa, X., Pérez-Rey, I., Alejano, L. R. & Masoumi, H. Size effects on strength and deformability of artificially jointed hard rock. *Int. J. Rock Mech. Min.* **176**, 105696 (2024).
16. Tuncay, E. & Hasancebi, N. The effect of length to diameter ratio of test specimens on the uniaxial compressive strength of rock. *B Eng. Geol. Environ.* **68**, 491–497 (2009).
17. Zhang, M., Lu, Y. J. & Yang, Q. Failure probability and strength size effect of quasi-brittle materials. *Chin. J. Mech. Eng.* **29**(9), 1782–1789 (2010).
18. Tang, C. A., Liu, H., Lee, P. K. K., Tsui, Y. & Tham, L. Numerical studies of the influence of microstructure on rock failure in uniaxial compression—part I: Effect of heterogeneity. *Int. J. Rock Mech. Min.* **37**(4), 555–569 (2000).
19. He, M. C., Li, C., Gong, W. L., Wang, J. & Tao, Z. Support principles of NPR bolts/cables and control techniques of large deformation. *Chin. J. Mech. Eng.* **35**(8), 1513–1529 (2016).
20. Greaves, G. N. et al. Poisson's ratio and modern materials. *Nat. Mater.* **10**(11), 823–837 (2011).
21. Pan, Y. S. *Coal Mine Rock Burst* (Science Press, 2019).
22. Li, Z. H., Guan, F. H. & Pan, Y. S. Analysis of stress field of rock surrounding circular roadway based on damage theory. *Rock Soil Mech.* **25**(S2), 160–163 (2004).
23. Wang, X. B., Pan, Y. S., Sheng, Q. & Ding, X. Numerical simulation on strain localization of end constraint of rock specimen. *J. Eng. Geol.* **10**(3), 233–236 (2002).
24. Liang, Z. Z., Xing, H., Wang, S. Y., Williams, D. J. & Tang, C. A. A three-dimensional numerical investigation of the fracture of rock specimens containing a pre-existing surface flaw. *Comput. Geotech.* **45**, 19–33 (2012).
25. Liang, Z., Wu, X., Tang, S. & Wang, W. Numerical simulation on end effect of rock specimens based on the anisotropic interface element model. *J. Basic Eng.* **26**(3), 526–537 (2018).
26. Wu, F. Q. et al. Uniaxial compression test study on size effect of small size rock samples. *Chin. J. Mech. Eng.* **40**(5), 865–873 (2021).
27. Xu, Y. H., Cai, M., Zhang, X. W. & Feng, X. T. Influence of end effect on rock strength in true triaxial compression test. *Can. Geotech. J.* **54**(6), 862–880 (2017).
28. He, M. et al. Dynamic properties of micro-NPR material and its controlling effect on surrounding rock mass with impact disturbances. *Undergr. Space* **15**, 331–352 (2024).
29. Ren, X., Zhang, X. & Xie, Y. Research progress in auxetic materials and structures. *Chin. J. Theor. Appl. Mech.* **51**(3), 656–689 (2019).
30. Chaurasia, A. & Walton, G. Laboratory and numerical modeling of the effects of width-to-height ratio on the strength and deformation behavior of pillars composed of porous, weak limestone. *Rock Mech. Rock Eng.* **57**(1), 719–738 (2024).
31. Rozhko, A. Y., Mews, K. S., Lozovyi, S. & Holt, R. M. Manifestation of negative microfracture compressibility due to capillarity in tight rocks at partial saturation with free gas. *Rock Mech. Rock Eng.* **57**, 9121–9143 (2024).
32. He, M. et al. Experimental study on the shear performance of quasi-NPR steel bolted rock joints. *J. Rock Mech. Geotech. Eng.* **15**(2), 350–362 (2023).

Acknowledgements

This work is supported in part by the National Natural Science Foundation of China (42272330) and Open Project of Collaborative Innovation Center of Mine Major Disaster Prevention and Environmental Restoration (CXZX-2024-15).

Author contributions

F.C. and J.D. wrote the main manuscript text. Y.D. prepared Figs. 1–15. All authors reviewed the manuscript.

Funding

Open Project of Collaborative Innovation Center of Mine Major Disaster Prevention and Environmental Restoration, CXZX-2024-15, National Natural Science Foundation of China, 42272330.

Competing interests

The authors declare no competing interests.

Additional information

Correspondence and requests for materials should be addressed to Y.D.

Reprints and permissions information is available at www.nature.com/reprints.

Publisher's note Springer Nature remains neutral with regard to jurisdictional claims in published maps and institutional affiliations.

Open Access This article is licensed under a Creative Commons Attribution-NonCommercial-NoDerivatives 4.0 International License, which permits any non-commercial use, sharing, distribution and reproduction in any medium or format, as long as you give appropriate credit to the original author(s) and the source, provide a link to the Creative Commons licence, and indicate if you modified the licensed material. You do not have permission under this licence to share adapted material derived from this article or parts of it. The images or other third party material in this article are included in the article's Creative Commons licence, unless indicated otherwise in a credit line to the material. If material is not included in the article's Creative Commons licence and your intended use is not permitted by statutory regulation or exceeds the permitted use, you will need to obtain permission directly from the copyright holder. To view a copy of this licence, visit <http://creativecommons.org/licenses/by-nc-nd/4.0/>.

© The Author(s) 2025